M. Quirino, L. Marocco, M. Guilizzoni, M. Lavagna
High Energy Rapid Modular Ensemble of Satellites Payload Thermal Analysis Using OpenFOAM
Journal of Thermophysics and Heat Transfer, Vol. 35, N. 4, 2021, p. 715-725
doi:10.2514/1.T6165

High energy rapid modular ensemble of satellites payload thermal analysis using OpenFOAM

Matteo Quirino*
Politecnico di Milano, Milano, Italy 20156

Luca Marocco†
Politecnico di Milano, Milano, Italy 20156

Manfredo Guilizzoni‡
Politecnico di Milano, Milano, Italy 20156

Michèle Lavagna§
Politecnico di Milano, Milano, Italy 20156

In a space mission design, the goal of the thermal control subsystem is to ensure that all components of the satellite stay within their operating temperature ranges. The problem becomes more critical if the mission involves nano-satellites with an astrophysics payload requiring a dedicated thermal design to keep it at low temperature, as in the case of the HERMES mission. Therefore, a thermal analysis is performed using ESATAN, one of the most used software packages among those suggested by ECSS. This gives a good overview of the temperature fields but many geometrical simplifications must be introduced in the model and all thermal interfaces must be checked. In order to asses the effect of the latter, the ESATAN results are cross-checked with those obtained using another software, OpenFOAM, in which the geometry is created directly from the CAD model of the satellite, resulting in a very accurate geometrical representation. By first comparing the view factors calculations against analytical test cases some issues emerged. These are thoroughly analyzed and discussed and it is finally shown that they do not affect the temperature field. The high level of detail of OpenFOAM highlighted interesting possible improvements in the thermal configuration of the satellite.

Nomenclature

CAD = Computer Aided Design

CFD = Computational Fluid Dynamics

ECSS = European Cooperation for Space Standardization

*Ph.D. Candidate, Department of Aerospace Science and Technology, Politecnico di Milano, via La Masa 34, 20156 Milano, Italy.
†Associate Professor, Department of Energy, Politecnico di Milano, via Lambruschini 4, 20156 Milan, Italy
‡Associate Professor, Department of Energy, Politecnico di Milano, via Lambruschini 4, 20156 Milan, Italy
§Full Professor, Department of Aerospace Science and Technology, Politecnico di Milano, via La Masa 34, 20156 Milano, Italy.

GCN = Gamma-Rays Coordinated Network

GMM = Geometrical Mathematical Model

GRB = Gamma Ray Burst

GUI = Graphical User Interface

LPA = Lumped Parameter Approach

PCB = Printed Computer Board

TP = Technological Pathfinder

SDD = Silicon Drift Detector

α_{vis} = absorptivity in the visible range

c_p = heat capacity

ε = emissivity

ε_{ir} = emissivity in the infra-red range

$F_{A_i - A_j}$ = view factor between face i and face j

k = thermal conductivity

$\hat{\mathbf{n}}_i$ = normal unit vector of face i

$\hat{\mathbf{n}}_j$ = normal unit vector of face j

q''' = heat flux per volume unit

q_s = external heat flux

ρ = density

$\mathbf{r}_j$ = position vector identifying points of face i

$\mathbf{r}_i$ = position vector identifying points of face j

$\mathbf{s}_{ij}$ = position vector from face i towards face j

σ = Stefan-Boltzmann constant

T = temperature

I. Introduction

A. HERMES mission

The HERMES mission is designed to create a constellation of six CubeSats of 3U size, in equatorial orbit at 550 km, with the main goal of detecting and triangulating Gamma Ray Bursts [1–5]. The mission is divided in two sets of 3 CubeSats each: the first three are named HERMES-TP, a technological path finder (TP) for the HERMES-SP [1–5] satellites that will integrate HERMES-TP with other three CubeSats of the same type, thus setting up the full HERMES constellation.

The detection of the Gamma Ray Burst is achieved through a scientific payload manufactured by INAF (Istituto Nazionale di Astrofisica) [1] (Fig. 1) which is able to record the energy time evolution of the event and to detect the time of occurrence of the observation. The location of the GRB on the celestial sphere is computed using the time and location of the satellites at the occurrence of the detection [6].

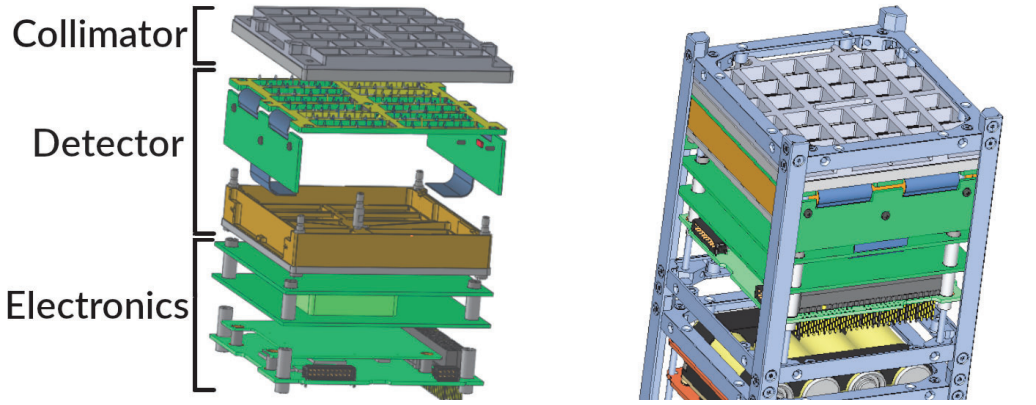

(a) INAF Payload (b) INAF Payload integrated in the service module

Fig. 1 INAF Gamma Ray Burst detector (courtesy of INAF-HERMES team)

The HERMES project involves European companies and universities. Among them, *Politecnico di Milano* (Polimi) has the task of designing the service module of the mission as well as integrating the INAF payload into the service module. The design involves the selection of all the hardware needed as well as its configuration inside the module, integration and testing. It requires the coordination of many subsystems, including the thermal control subsystem (TCS). This has the straightforward goal to keep all components within their operating temperature ranges for the entire duration of the mission. Particular attention must be paid to the scientific payload, which contains the silicon drift detector (SDD) [1] inside. To reduce the amount of current leakage, and thus the noise of the acquired data, this must be kept at a temperature below 0 °C but above −30 °C in order to avoid structural integrity problems.

In order to verify the temperature of the payload and of all the satellite components, a thermal analysis is performed. The article is focused on the HERMES-TP CubeSat which is modelled in ESATAN, one of the software tools suggested by the European Cooperation for Space Standardization* (ECSS) for thermal analyses. The required level of accuracy of the analysis is increased by the fact that the HERMES-TP mission involves 3U CubeSats, where all the hardware is stacked in a very small space (10 cmx10 cmx30 cm) and very close to each other. Therefore, small changes in the geometrical interfaces of the components might deeply affect the temperature of the parts nearby. The problem becomes more pressing by the presence of the astrophysics payload mounted onboard, which must be kept inside stringent temperature intervals. Consequently, the thermal analysis should precisely assess the conductive heat fluxes inside the CubeSat, in order to best predict the temperature coupling between the different components of the HERMES-TP

*https://ecss.nl/

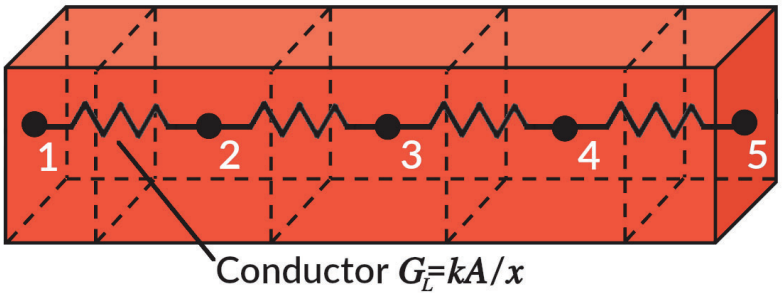

Fig. 2 Lumped Parameter Approach discretization of a bar into sections and respective nodes

satellite.

B. ESATAN model

The ESATAN software is based on the *Lumped Parameter Approach* (LPA) to compute the temperature field inside the satellite. The LPA involves modelling a continuous medium as a discrete network of *nodes*, representing the capacitance of the system, linked with each other by *conductors*, representing the conductance of the medium [7]. A detailed description of the method can be found in [8]. In order to set up a thermal network using the LPA, it is necessary to create in ESATAN the geometrical mathematical model (GMM) of the satellite [7]. The resulting model incorporates many simplifications with respect to the real satellite because of the complex geometry regions reductions [9].

The creation of the geometry in ESATAN implies the discretization of each component into sections, each of which is assigned a node. An example is shown in Fig. 2, where a bar is divided into 5 sections. The properties of each section such as thermal capacity, thermal conductivity, temperature, mass, are applied at the respective node (hence the term *Lumped Parameter*) [7]. The nodes are linked together by conductors. The heat is assumed to flow in one direction only from one section to the next one. Thus, for the simple case of Fig. 2 one node is linked to the next one by a conductance evaluated as [7]:

$$G_L = \frac{k\,A}{\Delta x} \tag{1}$$

where k is the thermal conductivity of the material between the nodes, A is the cross section area of the bar and Δx is the distance between the two adjacent nodes. The reader can refer to [10, 11] for the computation of conductances in more complex geometries, other than the simple cubic shape of this example. It should be pointed out that the creation of the GMM setup for a real model, e.g. the one shown in Fig. 3a and Fig. 3b, can take a lot of time.

The second step for building the network is to set the thermal connections between each part of the GMM. By default ESATAN considers the interfaces between two blocks as *fused*, i.e. in perfect thermal contact, as shown by the yellow line in Fig. 4. As a consequence, every interface for which a contact resistance should be specified (*contact* interface) needs to be manually identified. In the case of a real GMM, such as the one shown in Fig. 3b, for every component of

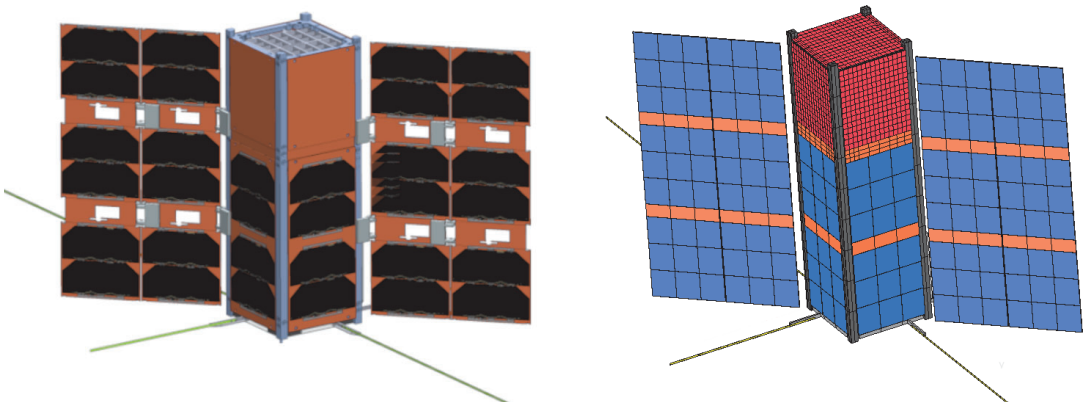

(a) HERMES-TP CAD model (b) ESATAN simplified geometry

Fig. 3 Overview of the HERMES-TP CAD model (left) and ESATAN geometry (right) (courtesy of Polimi-HERMES team)

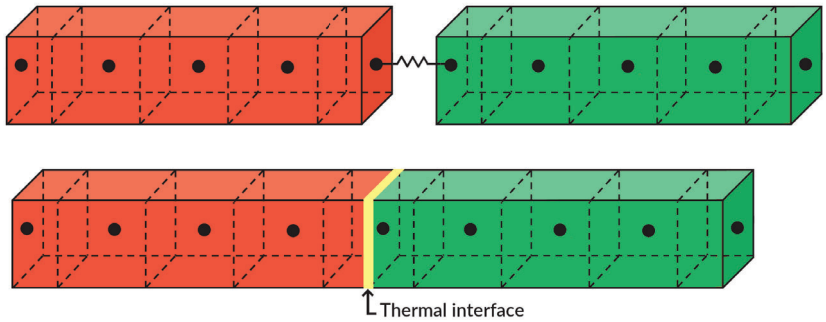

Fig. 4 Thermal interface created at the contact face between two bars using ESATAN

the CubeSat (e.g. PCB boards, structure, antennas, etc.) all thermal interfaces must be checked to either leave them as fused type (default) or to set them as contact interfaces with a proper value for the contact resistance. As can be inferred from Fig. 5, checking the correctness of every interface for a real CubeSat model is a highly time consuming task.

As a last step, the orbit and the attitude of the satellite are selected, so that the radiative input from the Sun and from Earth are taken into account.

The results computed in ESATAN provide a good overview of the temperatures of the CubeSat, allowing to spot criticalities in the different regions of the satellite. On the other hand, for a mission as HERMES-TP in which the accuracy of the thermal design is of paramount importance, it is necessary to assess the effect of the already cited simplifications. Therefore, there is the need of a tool that uses a high-fidelity geometrical model, reducing to a minimum the simplifications and that has a robust and less error prone set-up procedure, with respect to ESATAN, for the thermal interfaces. The selected tool is OpenFOAM, an open-source CFD software, that is able to compute view factors and the coupled radiative-conductive heat exchanges.

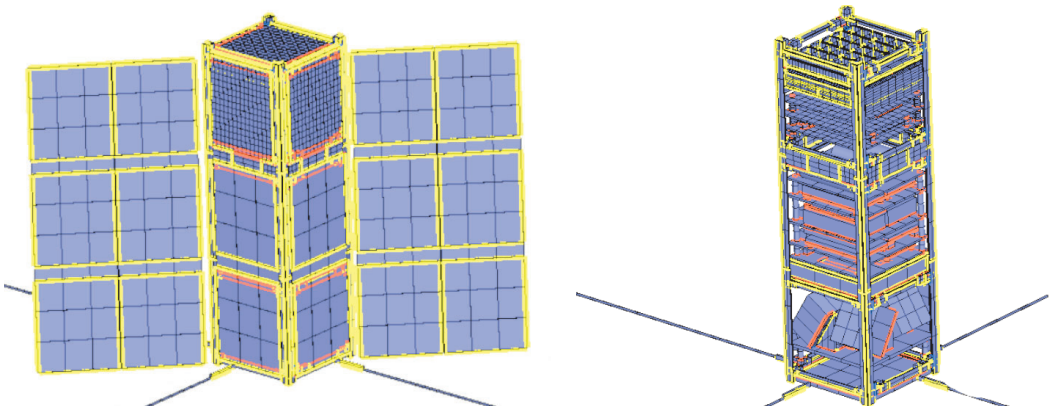

(a) (b)

Fig. 5 ESATAN model conductive interfaces: interfaces set as *contact* in orange, *fused* interfaces in yellow

II. OpenFOAM schemes and model

OpenFOAM is an open-source software programmed in C++ that implements the *Finite Volumes* method for the solution of thermo-fluid dynamics problems. More information on the software can be found in [12]. It includes utilities for pre-and post- processing, meshing and also for computing the view factors and the coupled radiative-conductive heat exchanges. Unfortunately, there is very little documentation that proves the correctness of such calculations. In Appendix IV a validation of the code against analytical test cases is discussed. As such validation proves to be successful, OpenFOAM confirms to be a promising tool to simulate the HERMES payload. Its results are compared with those obtained with ESATAN.

A. View Factors

The view factors are computed through the numerical evaluation of the double integral representing the energy exchange between two surfaces. A detailed description can be found in [13]:

$$F_{A_i-A_j} = \frac{1}{A_i}\int_{A_i}\int_{A_j}\frac{(\hat{\mathbf{n}}_i\cdot\mathbf{s}_{ij})(\hat{\mathbf{n}}_j\cdot\mathbf{s}_{ji})}{\pi S^4}dA_j\,dA_i \tag{2}$$

where $\mathbf{s}_{ij} = \mathbf{r}_j - \mathbf{r}_i = (x_j - x_i)\hat{\mathbf{i}} + (y_j - y_i)\hat{\mathbf{j}} + (z_j - z_i)\hat{\mathbf{k}}$, is the position vector connecting the points on face i with those on face j, S is the magnitude of $\mathbf{s}_{ij}$ and $\hat{\mathbf{n}}$ is the surface normal. The numerical integration is computed dividing the two surfaces into smaller subsurfaces [14]:

$$F_{A_i-A_j} \approx \frac{1}{\pi A_i}\sum_i\sum_j\frac{(\hat{\mathbf{n}}_i\cdot\mathbf{s}_{ij})(\hat{\mathbf{n}}_j\cdot\mathbf{s}_{ji})}{S^4}\Delta A_i\Delta A_j \tag{3}$$

If the two surfaces are flat rectangles and each is divided into N^2 subsurfaces, the expression inside the summation is evaluated N^4 times, thus the algorithm is of order $O(N^4)$ [14]. Due to the high computational demand, the view factors are not evaluated for each boundary cell face of the region for which radiation exchange is introduced. Instead, the boundary cell faces are grouped together, as exemplary shown in Fig. 6. Here, each cube side has 36 faces. The faces used to compute the view factors are agglomerated into groups of 2 faces each and the rays are shot for each of these groups. If a ray reaches another face after crossing a solid region, the destination face is excluded from the view factor computation as the two faces do not see each other along that direction. The effect of the resolution of the grouping on the values of the view factors is discussed in the following paragraphs.

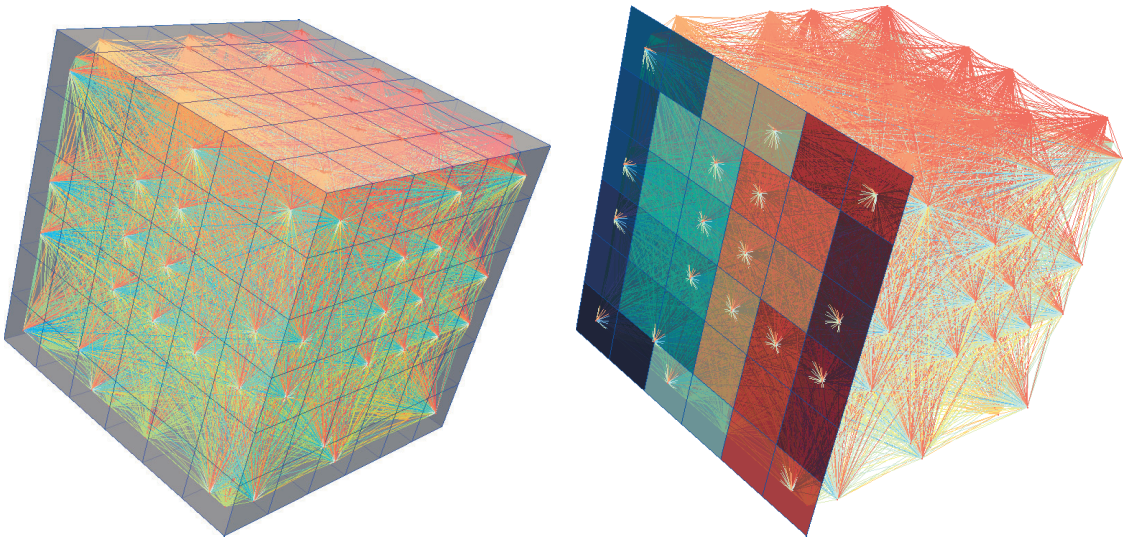

(a) Discretized faces and rays

(b) Boundary cell faces agglomerated into two faces for each group

Fig. 6 Rays and faces agglomeration used for the view factors computation

It should be noted that in Eq. (3) the term inside the summation has a lower limit of zero, occurring when the surfaces form grazing angles, so that the dot product becomes very small. On the other hand, there is no upper limit, meaning that if S^2 gets very small the summation might reach unrealistic high values, even bigger than one, which is physically not acceptable [8]. Such wrong values can be avoided if the finite differential areas ΔA_i and ΔA_j are small as well, balancing out the excessive increase due to the small value of S^2. It means that, as the distance between the two surfaces gets smaller, the discretization of the latter shall become finer.

The algorithm has been validated using cubic, spherical and cylindrical shapes and shells [15]. In Appendix IV.A it is reported the analytical cubic case, where it can be verified that as the distance D between the sides of the cube is reduced, the error in the calculation of the view factors increases, as previously discussed. On the other hand, as the number of cells on the sides of the cube is increased the error gets smaller, because the finite differential areas ΔA_i and ΔA_j become smaller, compensating the small distance D and thus reducing the error in the computation. This confirms

that, in order to properly compute the view factors, the number of discrete faces on a surface should be increased when the distance between two surfaces decreases, as thoroughly discussed in [15].

According to the discussion above, the computed view factors should always overestimate the correct values as the distance between the surfaces becomes smaller. Anyway, as shown for the sphere shell case reported in Appendix IV.B, it also happens that for some faces the correct analytical view factors are underestimated. The reason is that most of the rays shot from the agglomerated patches are at grazing angles to the surfaces from which they are shot from (e.g Fig. 21d). Consequently the related view factors are small, since $(\hat{\mathbf{n}}_i \cdot \mathbf{s}_{ij})$ and $(\hat{\mathbf{n}}_j \cdot \mathbf{s}_{ji})$ of Eq. (3) become very small. This results in having mostly small values and only a few big ones inside the summation of Eq. (3), thus leading to the underestimation of the view factor. The problem can be easily overcome by increasing the number of faces used to compute the view factors, thus increasing the resolution of the agglomeration. The effect is an increase of the number of generated rays *not* at grazing angles (e.g. Fig. 21b), so that the view factor value tends towards one, as it is expected for a convex surface radiating towards another one completely surrounding the first.

Another point to be clarified is that the number and dimensions, i.e. the resolution, of the faces used in the computation of the view factors, should be properly set for each case. Indeed, for a test case the analytical value of the view factor is known so that the resolution is set to reach such value. Anyway, for a complex geometry, the analytical value is not known *a priori*. The adopted resolution should thus ensure that all the view factors in the enclosure are close to 1. For the HERMES-TP mission, a 1U CubeSat structure from *ISIS-Space* has been used to find the proper resolution for ray casting. Two values have been compared: the lower one produced some faces in the enclosures with values above or smaller than 1, whilst for the higher resolution all faces in the enclosures are close to 1. Anyway, the difference in the temperature fields is around 0.01 K to 0.1 K so the lower resolution is good enough for the CubeSat geometry [15]. The time needed to compute the view factors is discussed in Section III.B.

In conclusion, increasing the overall cell number to obtain correct values for the view factors is not a good strategy as it will increase the computational cost. It works for the above test cases (e.g. Cubic test case) but it is much too expensive for a complex geometry. Inside the CubeSat there are many region and enclosures with small gaps between the components, with a high probability of computing some faces with view factors above 1. It is anyway shown in Section III that they do not significantly affect the computation of the temperature field inside the HERMES-TP payload.

B. Temperature Fields

The temperature fields are computed by solving the steady-state heat equation with uniform, isotropic and constant thermophysical properties. The source term accounts for the internal generation inside the CubeSat:

$$-k\nabla^2 T = q''' \tag{4}$$

Radiation acts at the boundaries of the solid regions. With reference to Fig. 7, at the far left of region (1) the following boundary condition (BC) is applied, where q_s is the incoming heat flux from the sun:

$$-k_1 \left.\frac{\mathrm{d}T}{\mathrm{d}x}\right|_{x=0} = q_s\,\alpha_1 - \frac{1}{A_1}\sum_{i=2}^{4} \frac{\sigma\left(T_1^4 - T_i^4\right)}{\left(\frac{1-\varepsilon}{\varepsilon A}\right)_1 + \frac{1}{A_1 F_{1-i}} + \left(\frac{1-\varepsilon}{\varepsilon A}\right)_i} \tag{5}$$

OpenFOAM requires the presence of a region in front of the face for which the view factors are computed and a temperature should be specified for the faces enclosing this region, as shown in Fig. 7.

For the solid-to-solid conduction the thermal conductivity and the thickness of a layer across the two solid regions should be specified. It is thus possible to simulate a contact thermal resistance between the components inside the satellite using the identity $h = k/L$, where h is the thermal contact coefficient [16]. The thin contact layer is not actually modelled in the mesh but it imposes the constraint of Eq. (6), as schematically shown in Fig. 7.

$$-k_1 \left.\frac{\mathrm{d}T}{\mathrm{d}x}\right|_{x=L_1} = -k_5 \left.\frac{\mathrm{d}T}{\mathrm{d}x}\right|_{x=L_1+L_c} = -\frac{k_c}{L_c}\left(T_{5c} - T_{1c}\right) \tag{6}$$

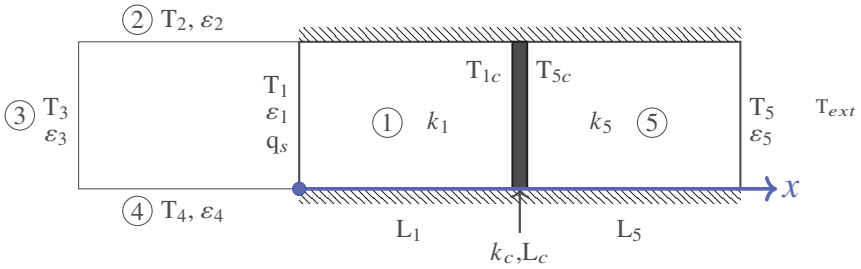

Fig. 7 Sketch of a simple model including radiative and conductive boundary conditions. The model is the same as that described in Appendix IV (Fig. 23)

The BCs have been first validated using 1D and 3D analytical test cases [15]. One of these is also reported in Appendix IV.C. It can be concluded that the they can be applied for the simulation of the thermal field of the HERMES-TP payload.

C. Numerical setup

The astrophysics payload of the HERMES CubeSat is the most important part of the satellite and the most critical from a thermal point of view, thus it is decided to focus the OpenFOAM analysis exclusively on such component. Furthermore, given the configuration of the payload unit inside the 3U CubeSat, the payload thermal problem is decoupled from the rest of the satellite. Limiting the analysis on the payload not only reduces the computational cost of the simulation, but it also highlights the conductive paths inside the detector and provides high-resolution results to crosscheck those from ESATAN.

As a first step the CAD model of the satellite is prepared for the thermal analyses, i.e. the geometrical details not relevant for the simulations, such as screws and screw fillets, are removed. The resulting CAD files, ready to be meshed, are showed in Fig. 9 and Fig. 10. The components analyzed are labelled with a reference number that will be used in the following sections.

The materials used in the simulation and their thermo-physical properties are listed in Table 1, PCB material properties computed as reported in [17]. The regions made of PCB material are colored in orange in Fig. 9 and Fig. 10 while those made of aluminum in light-grey. The same absorptivity in the visible range, α_{vis}, and the same emissivity in the infrared, ε_{ir}, are chosen for all materials. As shown in Fig. 8, the payload unit is placed inside a bounding box, simulating the space, whose thermal conductivity is set to zero for the simulations. A temperature of 0 K and an emissivity of 1 are assigned to the bounding surfaces. The empty space domain inside the CubeSat, shown in Fig. 8b, is needed to compute the view factors for the radiative exchange within the satellite. At the $-Y$ side of the CubeSat a heat flux q_S is imposed, simulating the incoming external solar radiation, as shown in Fig. 8a. Furthermore, a total heat source of 1 W is applied to all PCB boards labelled as (3), (4), and (6) in Fig. 9, simulating their power dissipation. In agreement with INAF, a value of h=100 W m^{-2} K^{-1} [16], evaluated as $h = k/L$ and thus setting k and L properly, is assigned to every contact resistance at the interface between the components.

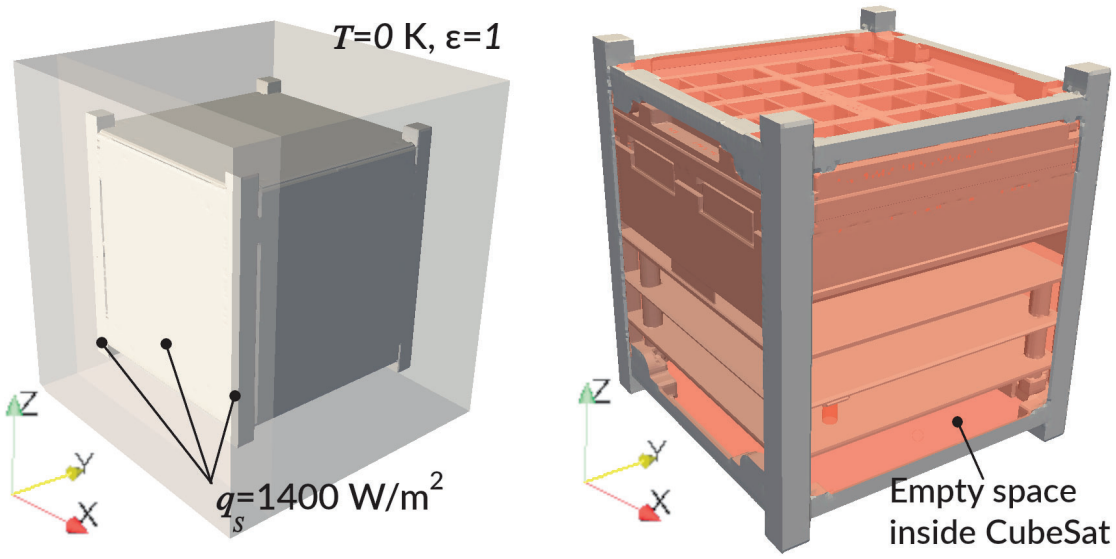

(a) Empty space around the CubeSat

(b) Empty space inside the CubeSat

Fig. 8 Empty spaces outside and inside the CubeSat used to compute the view factors

The domain is meshed with the standard meshing utilities of OpenFOAM, based on the creation of a background mesh and then the use of a trimmer to follow the CAD geometry, including refinement where needed. The resulting mesh has approximately 2.5 million cells. Of these, 1 million hexahedra cells pertains to the solid regions, in which

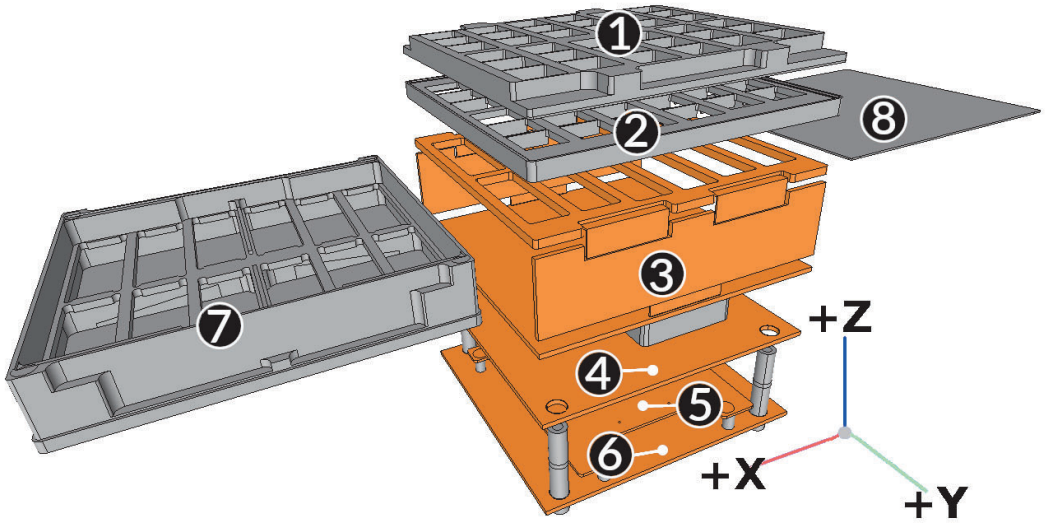

Fig. 9 Components inside the HERMES-TP payload unit (courtesy of INAF-HERMES team)

temperatures are computed (Fig. 11), while 1.5 million cells pertains to the empty domain regions (Fig. 8) needed only for the view factors computation. Indeed, the energy equation is not solved for these regions but they are anyway necessary to calculate the view factors before starting the simulation. Moreover, their bounding surfaces simulate the deep space at a temperature of 0 K for the radiative exchange of the satellite.

Table 1 Material properties used in the simulation

Material	α_{vis}	ε_{ir}	k [W m^{-1} K^{-1}]	c_p [J kg^{-1} K^{-1}]	ρ [kg m^{-3}]
Aluminum	0.86	0.86	220	910	2700
PCB	0.86	0.86	20	590	2200

As previously discussed, after generating the mesh the view factors are computed. An inspection of Fig. 12 and Fig. 13, reveals that several faces have values above 1, which is physically inconsistent. Indeed, the values in Fig. 12 and in Fig. 13, are the sum of all the view factors between the generic face and all the other faces it is able to see, so that the final value must be equal to 1 for an enclosure. As explained in Section II.A, the reason is the presence of short distances between the faces. Indeed, the values above 1 are found at the corners of the PCB boards (components (3), (4), and (6) in Fig. 12), which are close to the structural panels (components (9), (10), (12), and (13) in Fig. 10), and at the collimator fins (components (1) and (2) in Fig. 13) that are close to each other.

III. Results

The temperature field computed with OpenFOAM has a high level of detail, as shown in Fig. 14 - Fig. 17. From Fig. 14b it is possible to note how heat flows from the lower part of the PCB board (3) into the upper part. This latter is

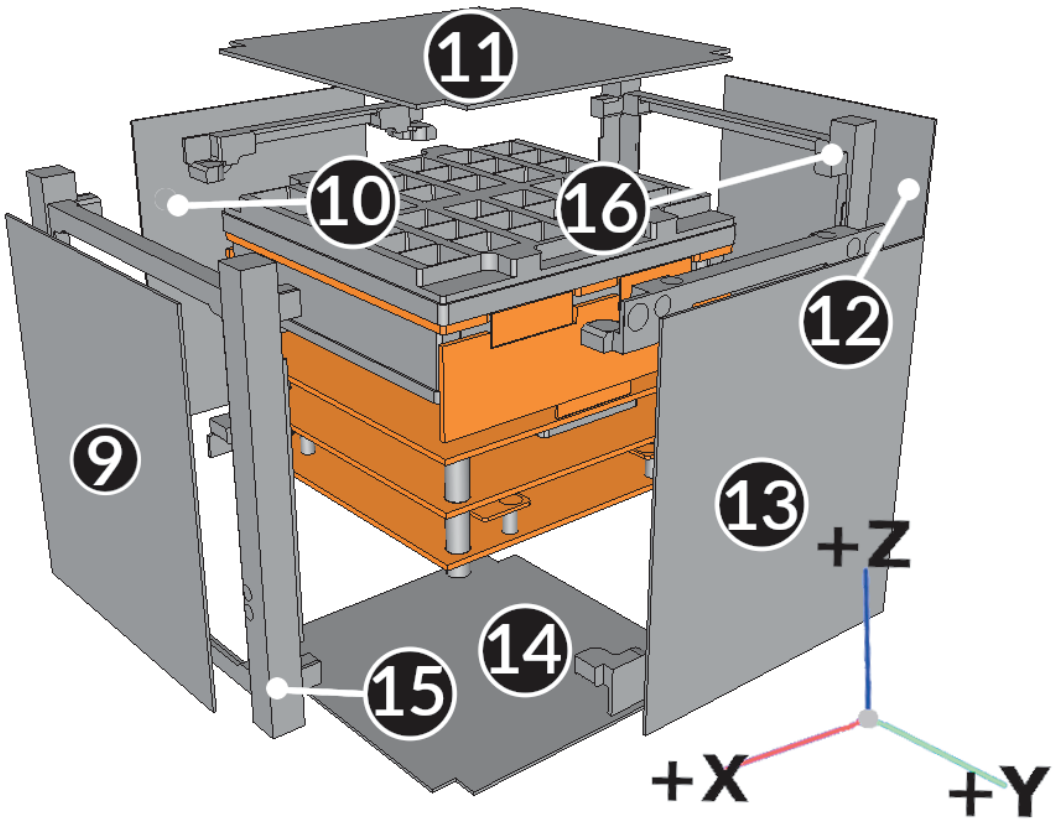

Fig. 10 Structural components of the HERMES-TP payload unit (courtesy of INAF-HERMES team)

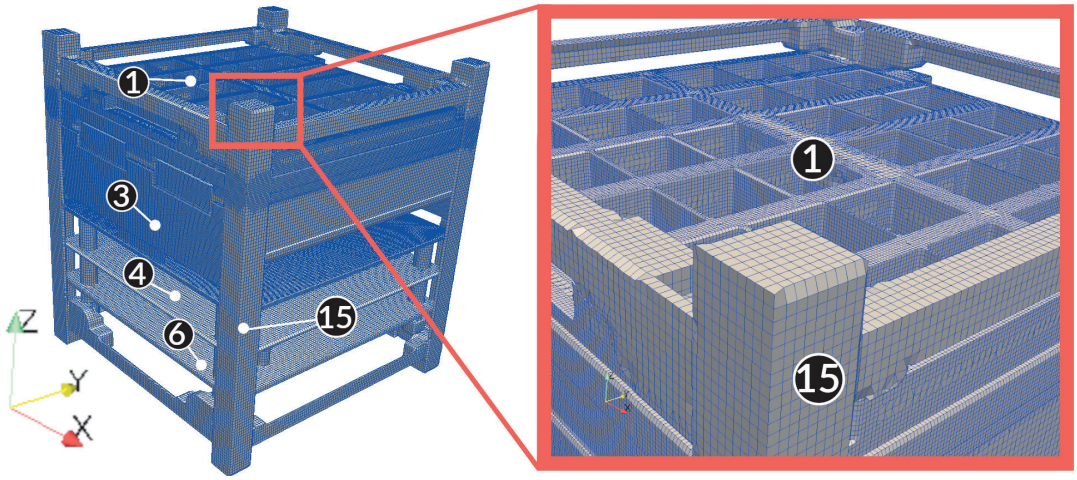

Fig. 11 Mesh produced in OpenFOAM

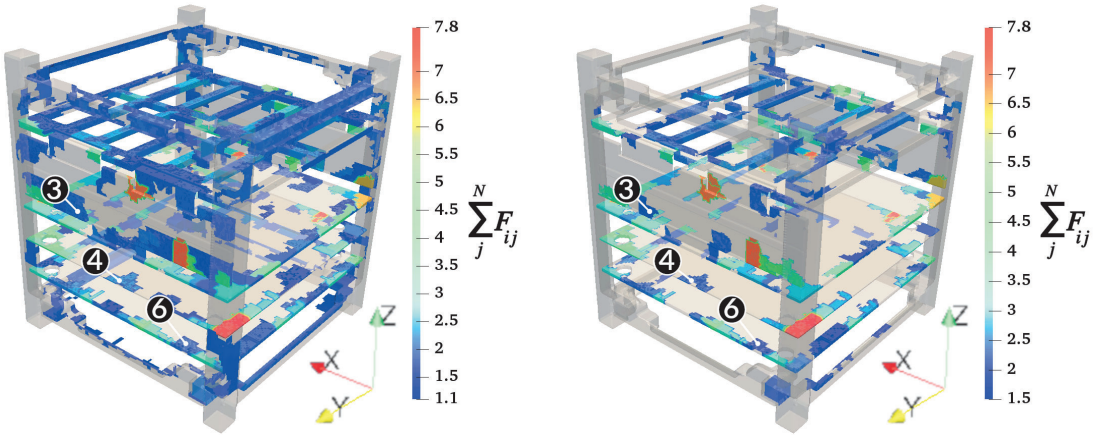

(a) Faces above 1.1 (b) Faces above 1.5

Fig. 12 Faces with view factors above 1 inside the CubeSat (all regions except the collimator)

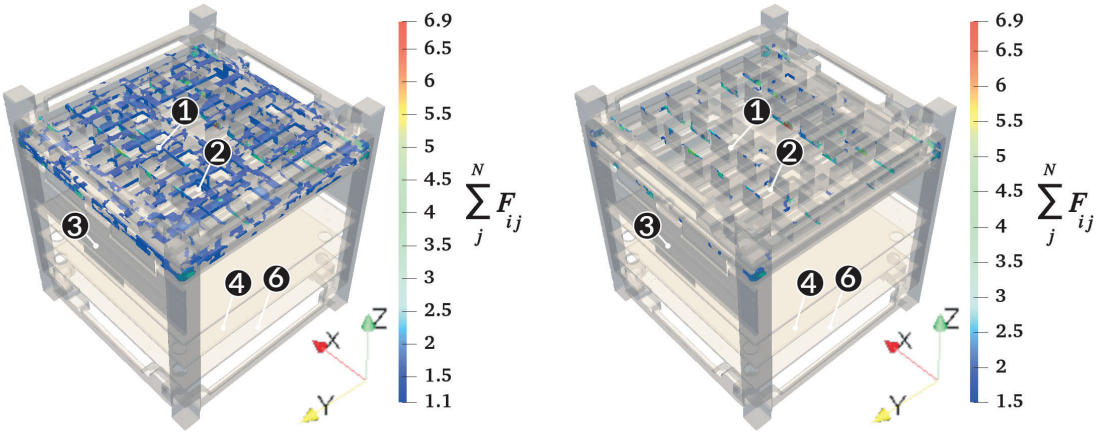

(a) Faces above 1.1 (b) Faces above 1.5

Fig. 13 Faces with view factors above 1 inside the CubeSat (collimator regions)

linked with the SDD (8), whose temperature must be kept within a narrow range around 0 °C. In order to reduce the heat flux coming from the lower part of component (3) from flowing upwards towards the SDD, thermal straps can be added between the latter and the structural panel (13). The heat flux path shown in Fig. 14b helps in determine the possible location of the thermal straps to obtain the maximum heat dump on the structural panel. As responsible for the payload design, INAF identified the red colored regions in Fig. 15 for the attachment of thermal straps. Anyway, the results obtained with the simulation show that those regions are actually not crossed by considerably high heat flux and thus are not the best placement for the thermal straps. Indeed, the lower board of component (3) before the connections with the upper part is a better location for the thermal straps. Here they prevent the heat generated in the lower part to flow into the upper part. INAF agrees with this solution and is presently implementing it. It is also important to avoid that the energy dissipated from the PCB board (4) flows as heat into board (3). The detailed results allowed to identify the best positions where to put the conductive pastes and thermal washers to let the heat flow downw towards the structure and preventing it from flowing upwards into PCB (3). Indeed, as highlighted in Fig. 16b by the red circles, part of the heat dissipated by board (4) flows towards the spacers connecting it to board (3). It is thus beneficial to place washers on the side of board (4) facing board (3) and conductive paste on the side facing board (6). Similar considerations hold for PCB (10), as shown by the red circles of Fig. 17b. The increased conductance due to the placement of washers or conductive paste in those regions has a double effect of reducing the temperature of the irradiated panel and the radiative heat flux towards the inside of the satellite, and increasing the heat dissipated on the shadowed panel.

A. Comparison with ESATAN

The results of the OpenFOAM simulations have been compared with those from ESATAN in order to assess the effects on the temperature fields of the geometrical simplifications. The only major differences between the temperature fields computed with the two codes are found in the collimator (1) and (2), as listed in Table 2. The reason is the different geometrical modelling between ESATAN and OpenFOAM. Indeed, in ESATAN the geometry has been simplified with respect to the real one. The temperature difference is due to the different contact areas between the two collimator regions and between the collimator and the structure. By looking at Fig. 18 it is possible to observe how the geometry of the collimator is precisely modelled in OpenFOAM, since it directly imports the CAD drawings of the CubeSat, with respect to the simplified geometry used in ESATAN.

The connection between the collimator and the structure is different in OpenFOAM and ESATAN, as shown in Fig. 18, being most likely the cause of the temperature difference. Furthermore, due to the different temperature of the collimators and thus to the different radiative heat exchange, also the +Z panel (11) shows a higher temperature difference between the two codes than that existing for the other panels (12)-(14).

As listed in Table 2, the temperature of the PCB boards matches between the two codes. This confirms that the faces with view factor values above 1, shown in Fig. 12 and in Fig. 13, have a negligible impact on the calculated

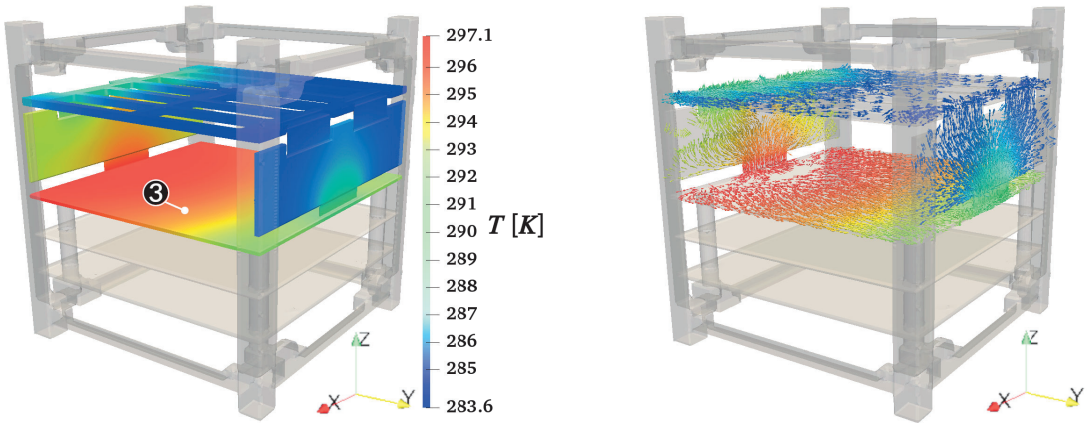

(a) Temperature distribution

(b) Heat flux path (normal vectors to isothermal lines)

Fig. 14 Temperature distribution and heat flux path for component (3) - Heat flowing from lower part of (3) towards upper part.

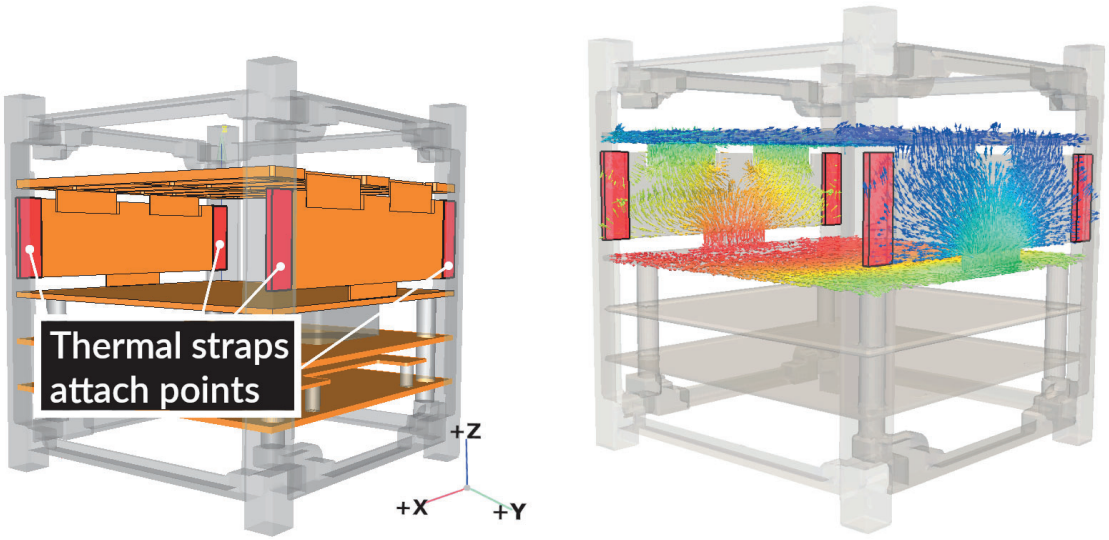

(a) Regions in which thermal straps can be attached (red color).

(b) Heat fluxes in the thermal strap attach points regions (red color).

Fig. 15 Locations on component (3) where thermal straps (red colored) can be attached and heat fluxes in such regions.

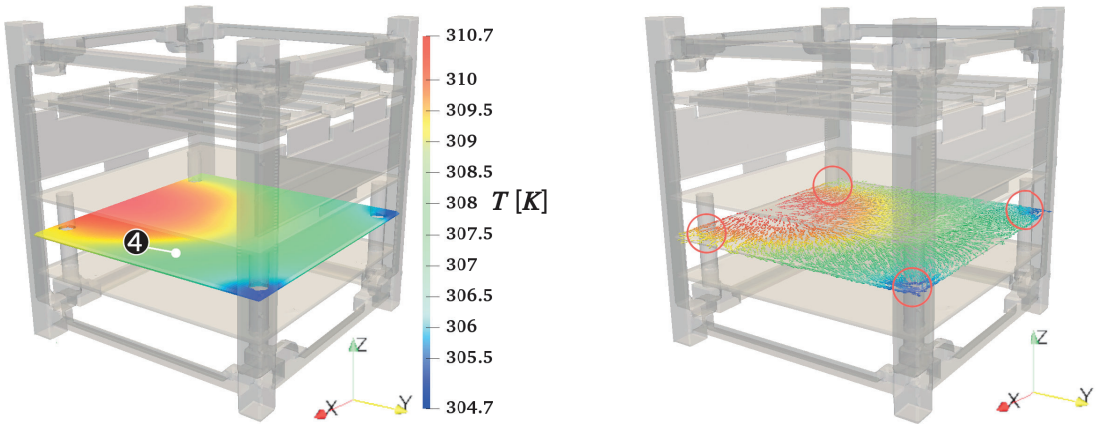

(a) Temperature distribution

(b) Heat flux path (normal vectors to isothermal lines)

Fig. 16 Temperature distribution and heat flux path for component (4)

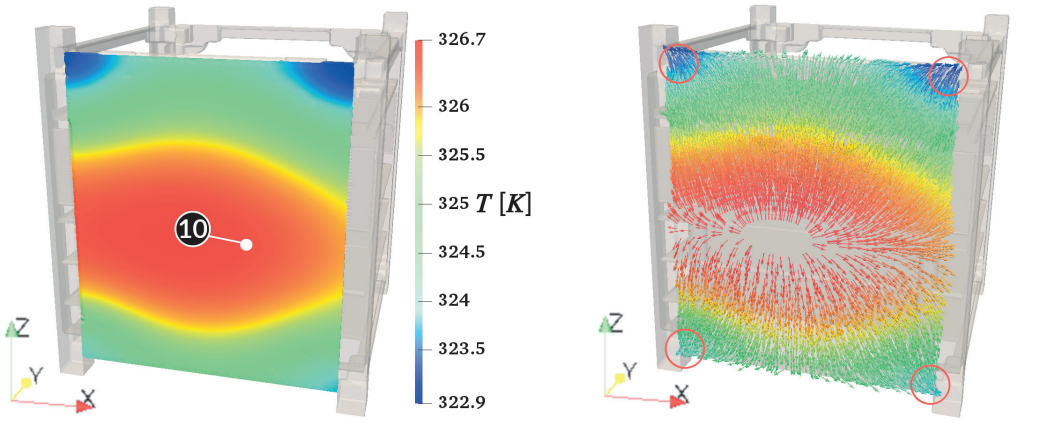

(a) Temperature distribution

(b) Heat flux path (normal vectors to isothermal lines)

Fig. 17 Temperature distribution and heat flux path for component (10).

Table 2 Comparison between OpenFOAM and ESATAN temperature predictions for the HERMES CubeSat payload unit (components numbers with reference to Fig. 9- Fig. 10). The last column refers to the absolute temperature difference between ESATAN and OpenFOAM for the maximum and minimum component temperature

	OpenFOAM [K]		**ESATAN [K]**		**$\|\Delta T\|$ [K]**	
Part	Min	Max	Min	Max	Min	Max
(1) **Collimator Top**	274.45	275.56	267.91	304.05	6.55	**28.49**
(2) **Collimator**	275.31	276.13	267.93	304.06	7.38	**27.93**
(3) PCB mask	283.60	297.14	288.24	297.39	4.64	0.25
(4) PCB PSU	304.64	310.71	305.74	310.35	1.09	0.36
(5) SmallPCB	318.36	321.45	317.12	319.56	1.24	1.90
(6) PCB PDHU	297.68	303.29	298.58	304.31	0.90	1.02
(7) Crystal Case	284.61	285.08	289.31	290.49	4.70	5.41
(8) SDD	284.04	284.49	288.15	288.31	4.11	3.82
(9) Panel+X	255.29	256.73	254.79	255.56	0.50	1.17
(10) Panel-Y	322.94	326.69	325.10	327.23	2.16	0.54
(11) Panel+Z	257.28	260.31	259.99	264.96	2.71	4.64
(12) Panel-X	254.70	256.09	254.91	255.67	0.21	0.42
(13) Panel+Y	252.35	253.10	253.05	253.53	0.71	0.43
(14) Panel-Z	261.36	264.86	262.61	266.63	1.25	1.77
(15) Rib+X	258.01	273.93	259.55	267.81	1.54	6.11
(16) Rib-X	257.70	272.14	259.55	267.81	1.85	4.33

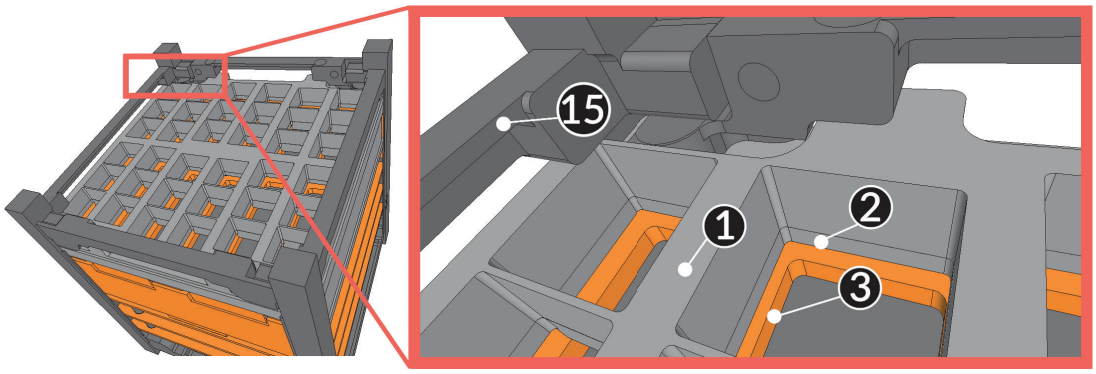

(a) Collimator geometry used in OpenFOAM

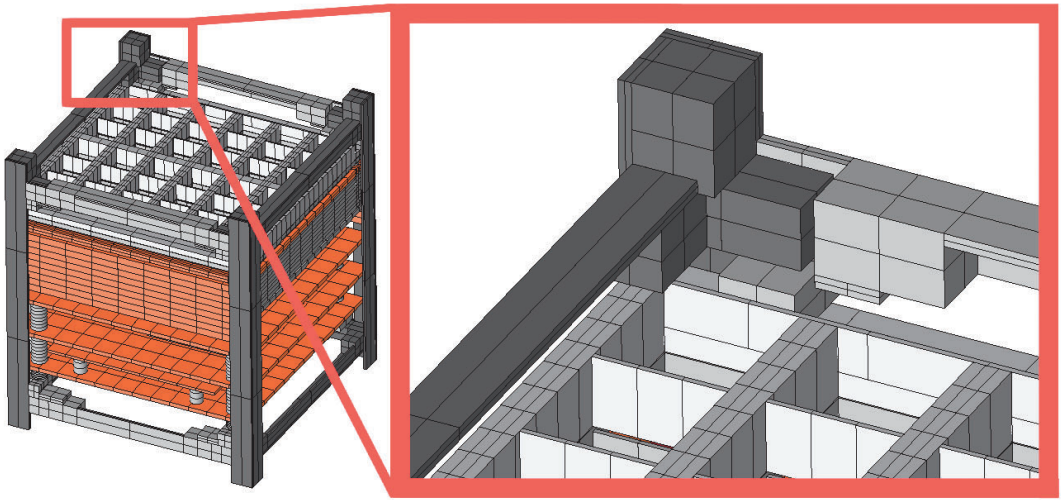

(b) Collimator geometry simplified in ESATAN

Fig. 18 Differences between the geometry used in OpenFOAM (top figure) and the simplified one used in ESATAN (bottom figure)

temperature fields. Furthermore, it also shows that the adopted ray casting resolution is appropriate. The discrepancy in the temperature of the collimator regions is thus not caused by the faces having view factors values above 1, otherwise also the temperature of the PCB boards would differ. The main reason for the discrepancy relies then in the geometrical simplifications.

B. Computational cost

The time required for an OpenFOAM simulation is much longer than that required by ESATAN. Considering 8 processors at 2.5 GHz, the HERMES payload unit requires around 15 min for the mesh generation, 50 min for the view factors computation (performed only once at the beginning) and approximately 10 h for the heat transfer simulation. On the contrary, the ESATAN model requires only 30 min to compute the steady state temperature field for the 25 000 nodes model of the HERMES payload unit, using a single processor. While OpenFOAM requires more time to compute the solution, ESATAN requires a long time to prepare the simplified model. The calculation times with OpenFOAM can however be reduced by using an arbitrary degree of parallelization.

IV. Conclusions

In the present paper the temperature field of a space satellite is calculated with two different codes, one based on the Lumped Parameter Approach (ESATAN) while the other on the Finite Volumes (OpenFOAM).

While ESATAN is well established in the space community for the thermal analysis of space components, it requires several geometrical simplifications. The open-source code OpenFOAM is then used to avoid such simplifications in the geometry and to assess their effects on the calculated temperature field.

Before applying OpenFOAM to the simulation of the HERMES-TP payload unit, its view factors calculation has been verified against analytical cases. It is shown that, even if in some situations unphysical view factors values above 1 appear, they do not affect the resulting temperature field.

Regarding the time required for a simulation, ESATAN runs much faster. Anyway, when considering the total time, comprising the geometry creation and the case setup, the two codes become comparable, if not even OpenFOAM faster.

Even though OpenFOAM does not incorporate an *Orbit Environment Simulator* as ESATAN does, the time varying radiative heat flux acting on the satellite can be easily implemented as boundary condition.

OpenFOAM has been proven to be well suited for the thermal analyses of space components. In fact, it allowed to identify possible changes to the HERMES-TP payload unit that did not emerge from the simulations performed with ESATAN, due to the excessive simplifications of the geometry.

For what concerns the future steps, it would be beneficial to modify the OpenFOAM code in order to retain only the relevant faces of the cells used for the view factors generation in the empty regions, instead of all the cells which are not used in the computation of the temperature fields. Furthermore, the implementation of thermo-mechanical features in

OpenFOAM, to perform high-resolution simulations including thermal stresses, would be very helpful. Indeed, many optical payloads are quite delicate from this point of view since small mechanical deformations might compromise the quality of the data produced by the instrument.

In conclusion, the cross check between the results from the two codes confirms the adequacy of OpenFOAM for thermal analyses of satellites with complex geometry and its usefulness to complete the commonly applied lumped parameter analyses.

Appendices

A. View factors for the "box" analytical test case

This appendix reports the results of the comparison between the view factors calculated using the analytical formulas and OpenFOAM for the case of one box (sketched in Fig. 19), where D assumes the different values reported in the tables below whilst the y and z dimensions of the cube are fixed to 1 m. The analytic equations have been taken from [16] and the tables report the absolute relative error between the analytical results and the OpenFOAM ones. As it can be observed in following tables if D becomes too small the view factors values go way above 1 for the reasons explained in Section II.A.

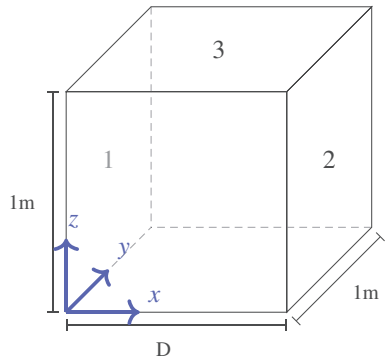

Fig. 19 Sketch of the domain for the "box" analytical test case

Table 3 View Factors for different values of D. Mesh resolution for the OpenFOAM calculation: 2 cells in x, 50 cells in y and z

2x50x50 cells	0.1 m			0.01 m			0.001 m		
	OF	Exact	Error%	OF	Exact	Error%	OF	Exact	Error%
F12	0.827 62	0.826 99	0.08	1.602 63	0.980 42	63	127.33	0.998 00	12 658
F13	0.044 11	0.043 25	1.98	0.004 88	0.004 90	3	0.000 08	0.000 50	84

Table 4 View Factors for different values of D. Mesh resolution for the OpenFOAM calculation: 2 cells in *x*, 100 cells in *y* and *z*

2x100x100 cells	0.1 m			0.01 m			0.001 m		
	OF	Exact	Error%	OF	Exact	Error%	OF	Exact	Error%
F12	0.827 15	0.826 99	0.02	1.009 43	0.980 42	3	31.85	0.998 00	3091
F13	0.043 35	0.043 25	0.23	0.005 57	0.004 90	14	0.000 16	0.000 50	69

B. View factors for the "sphere shell" test case

It is here analyzed the sphere shells test case showed in Fig. 20. The view factors have been generated for two configurations: one with low rays resolution, resulting in large errors, as reported in Table 6, the reasons explained in Section II.A, a second one with an higher resolution, that shows how rays are shot in more directions with respect to the previous configuration (see Fig. 21b vs. Fig. 21d) thus computing the correct values of view factors reported in Table 5. The cited tables report the absolute relative error between the analytical results and the OpenFOAM ones for different mesh sizes and the two different rays resolution: A high resolution with 1000 agglomerated faces and a low resolution with 100 agglomerated faces (refer to Sec. II.A for more details on how the faces are agglomerated by OpenFOAM [15]).

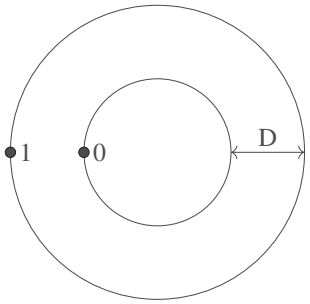

Fig. 20 Sketch of the domain for the "sphere shells" analytical test case

Table 5 Sphere shell view factors for D=0.1 m and 3 different mesh sizes – High rays resolution

0.1 m	**129 000 cells**			**428 000 cells**			**2 000 000 cells**		
	OF	Exact	Error%	OF	Exact	Error%	OF	Exact	Error%
F01	0.937	1.000	6	0.975	1.000	2	0.994	1.000	0.6
F10	0.849	0.902	6	0.865	0.902	4	0.895	0.902	0.8
F11	0.093	0.098	4	0.094	0.098	3	0.095	0.098	2

Table 6 Sphere shell view factors for D=0.1 m – Low rays resolution

0.1 m	**428 000 cells**		
	OF	Exact	Error%
F01	0.597	1.000	40
F10	0.473	0.903	48
F11	0.085	0.097	13

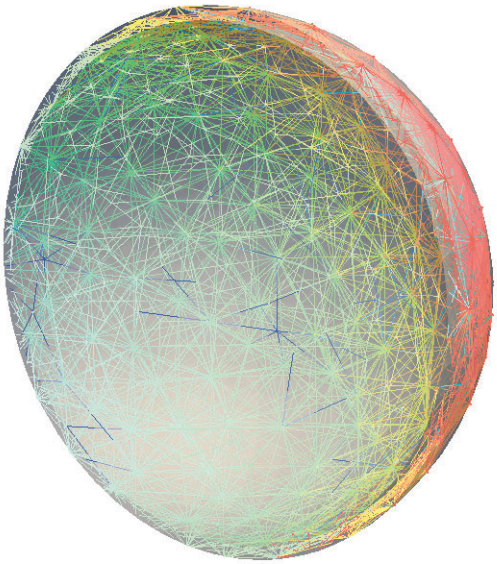

(a) High rays resolution inside the sphere shell

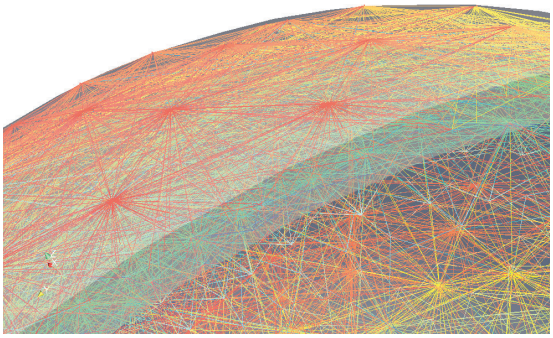

(b) Rays are shot in any direction, also perpendicular to faces

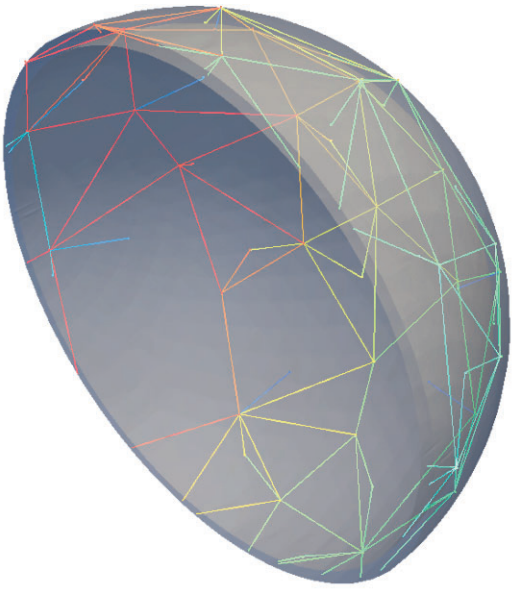

(c) Low rays resolution inside the sphere shell

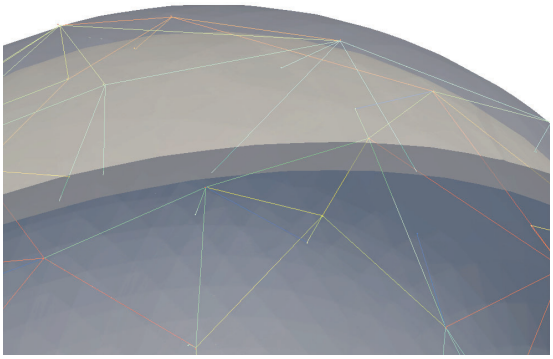

(d) Rays shot tangent to surfaces when using low resolution

Fig. 21 Rays shot for the sphere shells test case, high rays resolution (top figures) and low rays resolution (bottom figures)

C. Two-layer wall with contact resistance and radiation.

This third appendix presents the result concerning two analytical cases used to test the OpenFOAM boundary conditions to be used in the HERMES-TP model. The following tables report the analytically-calculated temperatures compared with the ones computed in OpenFOAM. The first case, pictured in Fig. 22 is used to test the solid-solid BC and as it is reported in Table 7, for a small ficticious layer with high conductivity the process takes more iteration with respect to the other cases, probably due to the small delta temperature across the layer. In the second case pictured in Fig. 23 along with the solid-solid BC also the radiative BC are tested. As it is reported in Table 7 - 8, both BC produce correct results, thus their application can be tested in more complex scenarios.

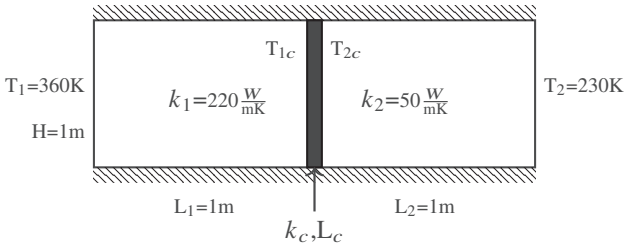

Fig. 22 1D fixed temperature multi region case; top and bottom boundaries are adiabatic.

Table 7 Fixed temperature 1D multi region results

L_c [m]	k_c [W m^{-1} K^{-1}]	T_{1c} [K]	T_{1cOF} [K]	T_{2c} [K]	T_{2cOF} [K]	ΔT_c [K]	ΔT_{cOF} [K]	Iters
1×10^{-6}	1×10^{-4}	342.90	342.81	305.26	305.11	37.63	37.69	1×10^5
1×10^{-6}	1×10^{-3}	336.87	336.73	331.78	331.63	5.09	5.10	1×10^5
1×10^{-6}	220.00	335.93	335.53	335.93	335.53	2×10^{-5}	-3×10^{-4}	4×10^6
1×10^{-1}	220.00	336.36	336.23	334.00	333.86	2.36	2.37	1×10^5

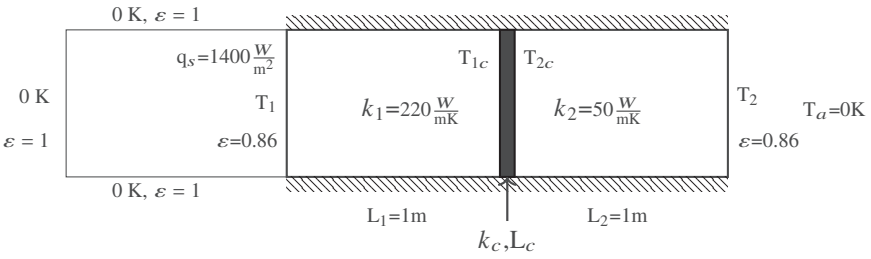

Fig. 23 1D radiation multi region case - Dummy fluid region on the left and external BC on the right

Table 8 1D radiation multi region results

h [W m^{-2} K^{-1}]	T_1 [K]	T_{1OF} [K]	T_2 [K]	T_{2OF} [K]
1×10^{-6}	338.55	338.57	327.85	327.83

V. Acknowledgments

The work of the the article has been possible thanks to the activities performed within the ASI (Agenzia Spaziale Italiana) grant n.2018-13-HH.O, “HERMES TP - Attività di Sistema” and thanks to the numerous iterations with the INAF-HERMES team.

References

[1] Fuschino, F., Campana, R., Labanti, C., Evangelista, Y., Feroci, M., Burderi, L., Fiore, F., Ambrosino, F., Baldazzi, G., Bellutti, P., Bertacin, R., Bertuccio, G., Borghi, G., Cirrincione, D., Cauz, D., Ficorella, F., Fiorini, M., Gandola, M., Grassi, M., Guzman, A., Rosa, G. L., Lavagna, M., Lunghi, P., Malcovati, P., Morgante, G., Negri, B., Pauletta, G., Piazzolla, R., Picciotto, A., Pirrotta, S., Pliego-Caballero, S., Puccetti, S., Rachevski, A., Rashevskaya, I., Rignanese, L., Salatti, M., Santangelo, A., Silvestrini, S., Sottile, G., Tenzer, C., Vacchi, A., Zampa, G., Zampa, N., and Zorzi, N., *HERMES: An ultra-wide band X and gamma-ray transient monitor on board a nano-satellite constellation*, Vol. 936, Elsevier B.V., 2019. https://doi.org/10.1016/j.nima.2018.11.072, iSSN: 01689002 Publication Title: Nuclear Instruments and Methods in Physics Research, Section A: Accelerators, Spectrometers, Detectors and Associated Equipment.

[2] Scala, F., Zanotti, G., Curzel, S., Fetescu, M., Lunghi, P., Lavagna, M., Lavagna, M., and Bertacin, R., "The HERMES mission: a CubeSat constellation for multi-messenger astrophysics," 2020.

[3] Colagrossi, A., Prinetto, J., Silvestrini, S., Orfano, M., Lavagna, M., Fiore, F., Burderi, L., Bertacin, R., and Pirrotta, S., "Semi-Analytical Approach to Fasten Complex and Flexible Pointing Strategies Definition for Nanosatellite Clusters: The HERMES Mission Case from Design to Flight," 2019. URL http://hdl.handle.net/11311/1118852.

[4] Colagrossi, A., Prinetto, J., Silvestrini, S., and Lavagna, M. R., "Sky visibility analysis for astrophysical data return maximization in HERMES constellation," *Journal of Astronomical Telescopes, Instruments, and Systems*, Vol. 6, No. 4, 2020, p. 048001. https://doi.org/10.1117/1.JATIS.6.4.048001, URL https://www.spiedigitallibrary.org/journals/Journal-of-Astronomical-Telescopes-Instruments-and-Systems/volume-6/issue-4/048001/Sky-visibility-analysis-for-astrophysical-data-return-maximization-in-HERMES/10.1117/1.JATIS.6.4.048001.short, publisher: International Society for Optics and Photonics.

[5] "H.E.R.M.E.S.: a CubeSat Based Constellation for the New Generation of Multi-Messenger Astrophysics," , Nov. 2020. URL https://re.public.polimi.it/handle/11311/1146023#.X79yE8J7mCg.

[6] Hurley, K., Briggs, M. S., Kippen, R. M., Kouveliotou, C., Fishman, G., Meegan, C., Cline, T., Trombka, J., McClanahan, T., Boynton, W., Starr, R., McNutt, R., and Bor, M., "The interplanetary network supplement to the burst and transient source experiment 5B catalog of cosmic gamma-ray bursts," *Astrophysical Journal, Supplement Series*, Vol. 196, No. 1, 2011. https://doi.org/10.1088/0067-0049/196/1/1.

[7] "ESATAN-TMS Thermal Engineering Manual," Tech. rep., 2015.

[8] Incropera, F. P. (ed.), *Fundamentals of heat and mass transfer*, 6th ed., John Wiley, Hoboken, NJ, 2007. OCLC: ocm62532755.

[9] Nijenhuis, A. K. t., Brouwer, H. S. B., Jonsson, M., Bloem, E. A., Benthem, R. C. v., and Volmuller, G. J., "Thermal Modelling of CubeSats in ESATAN-TMS," 2020. URL https://reports.nlr.nl/handle/10921/1542, accepted: 2020-10-07T12:59:41Z Publisher: Netherlands Aerospace Centre NLR.

[10] Appel, S., Patrício, R., de Koning, H. P., and Pin, O., "Automatic Conductor Generation for Thermal Lumped Parameter Models," 2004, pp. 2004–01–2397. https://doi.org/10.4271/2004-01-2397, URL https://www.sae.org/content/2004-01-2397/.

[11] "ESATAN-TMS Workbench User Manual," Tech. rep., 2017.

[12] OpenFOAM, *Main Page — OpenFOAM Wiki,*, 2019. URL https://wiki.openfoam.com/index.php?title=Main_Page&oldid=2897.

[13] Modest, M. F. M. F., *Radiative heat transfer*, Elsevier Science, 2013.

[14] Walton, G., "Calculation of obstructed view factors by adaptive integration," Tech. Rep. NIST IR 6925, National Institute of Standards and Technology, Gaithersburg, MD, 2002. https://doi.org/10.6028/NIST.IR.6925, URL https://nvlpubs.nist.gov/nistpubs/Legacy/IR/nistir6925.pdf.

[15] Quirino, M., "Thermal analysis of HERMES-TP CubeSat using ESATAN and OpenFOAM," , Dec. 2019. URL https://www.politesi.polimi.it/handle/10589/151674.

[16] Lienhard, J. H., and Lienhard, J. H., *A heat transfer textbook*, 4^{th} ed., Dover Publications, Mineola, N.Y, 2011. OCLC: ocn630478192.

[17] Chandrashekar, S., Berggren, A., and Karlsson, T., "Thermal Analysis and Control of MIST CubeSat," , 2016. URL http://www.diva-portal.org/smash/get/diva2:1071655/FULLTEXT02.